

Brewers' Spent Grains-Derived Carbon as Anode for Alkali Metal-Ion Batteries

Sandesh Darlami Magar, Christian Leibing, Juan Luis Gómez-Urbano, Daniel Carriazo, and Andrea Balducci*

Herein, the synthesis of a nongraphitizable carbon through cost-effective pyrolysis of a brewery waste product is reported. It is demonstrated that it is possible to realize hard carbon (HC) with structural and morphological properties from an abundant biomass source with a suitable application in energy storage devices. Resulting HC displays reversible capacities of 334, 112, and 140 mAh g⁻¹ after 100 cycles at 1C with high charge/discharge efficiency (>99.6%) in Li-ion, Na-ion, and K-ion batteries, respectively. Thus, HC derived from brewers' spent grains can be considered as promising materials for the realization of advanced metal-ion batteries.

1. Introduction

The development of efficient and sustainable energy storage devices is of crucial importance for the future of our society. Batteries and supercapacitors are the most utilized energy storage devices in our daily life and they are nowadays used in a large number of applications, ranging from portable devices to transportations.^[1,2] The number of these applications is continuously increasing, and in the future, it will be essential to improve not only the performance (energy density, power density, safety, cycle life) of these energy storage devices, but also their sustainability in terms of (renewable) sources, availability,


and recyclability. This overall improvement can only be achieved through an accurate selection of the materials, actives, and inactives, used in these devices.

Carbon is one of most versatile and well-established material in energy storage devices. Carbon-based materials are widely investigated as active and inactive electrode material (functional additives) in batteries and supercapacitors. They show a wide range of structural properties such as crystallinity (degree of graphitization), amorphicity, various morphologies (0D nanospheres, 1D nanotubes, 2D graphene,

3D bulky porous carbon), and surface functionalities.^[3] In alkali metal-ion batteries, carbon materials such as graphite, soft carbon, and hard carbon (HC) exhibiting intercalation properties are common, while carbons like 3D bulky porous carbon, graphene, carbon nanotubes with high surface area are utilized in supercapacitors. Nongraphitizing carbons, such as HCs, are presently considered as one of the most interesting materials for the realization of high-performance and sustainable energy storage devices.^[4,5] These carbons are normally synthesized through a relatively simple synthesis route, based on heat treatment of a carbon-rich precursor (natural or artificial in origin) at temperatures usually above 500 °C under inert atmosphere. The control of synthesis parameters, such as annealing temperature, inert gas flow, and temperature, makes possible a tuning of the carbon properties in terms of porosity, heteroatoms content, and degree of graphitization.^[6,7] When used as active material, HC allows the realization of composite electrodes able to display high specific capacity, long cycling stability, and good rate performance in lithium-/sodium-/potassium-ion batteries (LIBs, NIBs, and KIBs, respectively).^[8–11] One of the challenges related to the practical application of HC-based electrodes lies in their low initial charge/discharge efficiency. In order to overcome this drawback, it is extremely important to understand and precisely control the structure and functional properties of these materials, which are the origin of their electrochemical behavior.^[4,12,13] Generally, the storage of alkali metal ion in nongraphitizing carbon is believed to be different than stage intercalation of lithium in graphite to which many proposals^[14–17] have been put forth to explain it. Three phenomena discussed commonly in literature are adsorption, intercalation, and pore filling mechanism at various potential ranges. The adsorption phenomenon is a binding of metal ion into defective sites, edges, heteroatoms, and functional groups, which are considered as an energetically favorable process occurring in higher voltage region versus reference metal (M⁺/M).

S. D. Magar, C. Leibing, A. Balducci
Institute for Technical Chemistry and Environmental Chemistry and Center for Energy and Environmental Chemistry Jena (CEEC Jena)
Friedrich Schiller University Jena
Philosophenweg 7a, 07743 Jena, Germany
E-mail: andrea.balducci@uni-jena.de

J. L. Gómez-Urbano, D. Carriazo
Centre for Cooperative Research on Alternative Energies (CIC energiGUNE)
Basque Research and Technology Alliance (BRTA)
Alava Technology Park, Albert Einstein 48, 01510 Vitoria-Gasteiz, Spain
D. Carriazo
IKERBASQUE, Basque Foundation for Science
48013 Bilbao, Spain

 The ORCID identification number(s) for the author(s) of this article can be found under <https://doi.org/10.1002/ente.202200379>.

© 2022 The Authors. Energy Technology published by Wiley-VCH GmbH. This is an open access article under the terms of the Creative Commons Attribution-NonCommercial License, which permits use, distribution and reproduction in any medium, provided the original work is properly cited and is not used for commercial purposes.

DOI: 10.1002/ente.202200379

Intercalation refers to the insertion of the metal ions within the layer structure of the graphitic domain, while during pore filling, metal ions form clusters inside the pores (diameter < 20 Å).

Due to the favorable features mentioned above, the number of investigations dedicated to HC derived from biomass has risen significantly in the past decade (see Figure S1, Supporting Information). So far, a large variety of biomass have been used as precursors for HC,^[4,18] for example, banana peels,^[19] Lotus stem,^[20] and potato^[21]-derived HC are reported as most promising anodic materials for LIBs, NIBs, and KIBs respectively. It has been shown that the characteristics of the utilized biomass affect the morphological and structural properties of HCs and, at the same time, that the use of natural precursors leads to the formation of materials displaying structural and functional inhomogeneity.^[18] These latter are caused by the variable nature of the precursors and represent an aspect which needs to be carefully considered during the development of HC suitable for energy storage devices.

Plant derivatives are among the most available biomasses of which a huge portion is represented by the agricultural and food industry waste matter. Brewer's spent grain (BSG) is a common agro-industrial biowaste. It is a byproduct generated in breweries after the extraction of wort during preliminary operation called mashing process. BSG is a major waste, which roughly represents about 85% of total byproducts during brewing and roughly 20 kg of wet BSG are produced per 100 L of brewed beer.^[22] About 6.8 billion tons of wet BSG is produced in EU (2019 data). Germany alone contributed ≈1.5 billion tons of wet BSG in 2019.^[23] BSG is proving to be largely available, easy to process, and logistically advantageous compared with the biomass precursors that are generated as household waste or in the wild such as banana peels, waste tea bag, apple waste, plant parts, etc. The BSG is primarily composed of cellulose, hemicellulose, and lignin and additionally nonlignocellulose components such as starch, proteins, ash, etc. are present, while the actual composition may fluctuate depending on factors such as harvesting time and processing.^[24] It is interesting to notice that despite this large availability, so far only one study^[25] has been dedicated to the use of BSGs as precursors of HC and this material has only been applied in NIBs. Thus, the study of these promising precursors for LIBs, SIBs, and KIBs with the aim to explore their electrochemical performance and understand their mechanistic insights appears as a topic of great interest.

Herein, we report a simple, cheap, and green synthetic approach for the preparation of a HC derived from the pyrolysis of BSG and its further evaluation versus lithium, sodium, and potassium in a half-cell configuration. The derived BSG HC with

low Brunauer, Emmett, and Teller (BET) surface area and extended graphitic interlayer exhibits high capacity and excellent capacity retention in lithium- and sodium-ion cell. In addition, the trend of metal-ion mobility suggests a kinetically favored pore filling of sodium and potassium in derived HC offering higher rate performance.

2. Experimental Section

2.1. Material Synthesis

Fresh wet BSG was collected from a local brewery in Jena, Germany, and to avoid the microbial decomposition, the precursor was dried at 80 °C for 48 h. Subsequently, the dried precursor was ground using mortar and pestle. The powder precursor was pyrolyzed in a tubular furnace under constant flow of nitrogen gas (110 cc min⁻¹) by heating to 1000 °C with a heating rate of 500 °C h⁻¹ and holding this temperature for 3 h. The resulting carbon was ball milled with a rotational speed of 500 rpm for 4 h in a planetary ball mill (Pulverisette 6, Fritsch). The yield was 23% (Figure 1).

2.2. Material Characterization

Thermogravimetric analysis (TGA) and differential thermal analysis (DTA) of BSG precursor were carried out in a Perkin Elmer STA 600 under constant flow of air or nitrogen. To reduce the air content for the latter measurement, the sample was vacuum dried at 60 °C and loaded into a crucible (under argon atmosphere). The morphology of the carbon particle was studied using a scanning electron microscope (SEM). The elemental composition was determined using energy-dispersive X-ray spectroscopy (EDX) using a Phenom ProX scanning electron microscope at acceleration voltage 15 kV. An Autosorb iQ3 machine from Quantachrome Corporation was used for nitrogen physisorption measurement. The specific surface area was calculated using BET method. Raman spectra were collected using an InVia confocal Raman microscope from Renishaw with excitation at wavelength of 532 nm. The Raman intensity ratio (I_D/I_G) of the carbon sample was calculated from the deconvoluted peaks of D- and G-band using Lorentzian fit (OriginPro software), as shown in Figure S4b, Supporting Information.

2.3. Electrochemical Preparation and Testing

The electrodes were prepared by casting a slurry containing the synthesized HC, conducting carbon (Super C60, Imerys), and

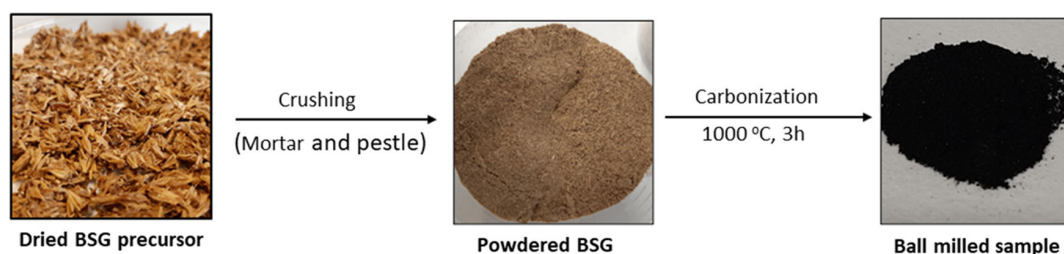


Figure 1. Schematic diagram of HC synthesis from dried BSG precursor.

carboxymethyl cellulose (CRT 2000 Walocel) dissolved in water (with a ratio 90:5:5), upon copper foil. The film was dried at room temperature and, afterward, punched into 12 mm-diameter disc-shaped electrodes. The mass loading of the electrodes was below 1 mg cm^{-2} . Vacuum drying of electrodes at 80°C for 24 h was performed before transferring them inside an argon filled glovebox (M Braun) with O_2 and H_2O level below 1 ppm. Swagelok-type cells were utilized for all the electrochemical investigations reported in this study. All tests were carried out utilizing a three-electrode cell setup. The HC-based electrodes were used as working electrode, while metallic Li/Na/K was used as counter electrode. The metal utilized as a counter was also used as reference. A glass microfiber filter (Whatman GF/D) soaked with $150 \mu\text{L}$ electrolyte was used as a separator.

A solution of 0.9 M "X" bis-fluorosulfonylimide (FSI), with $\text{X} = \text{Li}, \text{Na}, \text{K}$, (LiFSI and KFSI purchased from Solvionic, NaFSI from BLD Pharmatech) dissolved in a mixture of propylene carbonate (PC, anhydrous 99.7 %, Sigma Aldrich) and tetraethoxy-glyoxal (TEG, supplied by Weylchem, purified by overpressure Schlenk filtration over dried aluminumoxide) (7:3 by wt%) and containing 2% by vol. of vinyl ethylene carbonate (VEC, Sigma Aldrich) was used as electrolyte. In the following the electrolytes will be indicated as 0.9 M XFSI in PC/TEG (3:7).

The galvanostatic charge/discharge and cyclic voltammetry (CV) measurement were performed using an Arbin Instruments LBT21084 and an MPG-2 (BioLogic) at room temperature. The tests were carried out in the potential range between 0.005 and 2.5 V versus reference metal (M^+/M). All electrochemical tests were conducted at room temperature. Galvanostatic charge/discharge was carried out utilizing current densities of 0.1C, 0.5C, and 1C (with $1\text{C} = 0.372 \text{ A g}^{-1}$). The cyclic voltammetry measurement was carried out at a scan rate of 0.1 mV s^{-1} .

The mobility of the metal ion inside the carbon electrode was investigated using galvanostatic intermittent titration (GITT). In this technique, short current impulses were applied to the cell and the voltage response with respect to time was recorded, both during the current impulse and over the relaxation period, when no current passed. Under the assumption of Fick's second law, the diffusion coefficient obtained after solving the equation^[26] is given by

$$D = \frac{4}{\pi\tau} \left(\frac{m_B V_m}{M_B S} \right)^2 \left(\frac{\Delta E_s}{\Delta E_t} \right)^2 \left(\tau \ll \frac{L^2}{D} \right) \quad (1)$$

where m_B is the mass, V_m is the molar volume, M_B is the molar mass of active material, τ is the relaxation time, S is the surface area of the electrode, F is the Faraday constant, n is the number of electrons, ΔE_s is the change of steady-state voltage at the end of the relaxation period, and ' ΔE_t ' is the total change in cell voltage during current pulse, neglecting ohmic resistance (IR) drop.

3. Results and Discussion

The thermal decomposition of the precursor (Figure 2a) can be divided into three main stages. The early stage of slow weight loss below 200°C can be associated with evolution of volatile compounds adsorbed on the surface of the precursor, mainly water. The second stage consists of a fast weight loss of about 50 wt% between 200 and 350°C . It is accompanied with exothermic peaks corresponding to hemicellulose decomposition at lower-temperature range of $220\text{--}315^\circ\text{C}$ and cellulose decomposition at temperature range of $315\text{--}400^\circ\text{C}$. The third stage showcases the decomposition of lignin, which is rather slow and occurs at wider ranges of temperature starting from 200 to 800°C .^[27,28] From these results the lignin content of the BSG precursor is estimated between 35 and 45% of the total mass while the overall cellulosic component (cellulose and hemicellulose) between about 40 and 50%. The ash content of the sample represents 5 wt%.

The morphology of HC with bulky and dense surfaces is similar to high lignin-based biomass-derived HC.^[25,29] This observation supports the relatively higher lignin content of the precursor estimated in TGA. The particle size ranges from few micrometers to $40 \mu\text{m}$ (Figure 2b). To acquire the porosity of the HC, N_2 physisorption measurement was carried out, which shows typical curve of type II isotherm (Figure 3c), a characteristic of nonporous material in which the adsorption at low relative pressure is very low, so, as in most of the HCs, the major adsorption is mainly associated with the adsorption on the external surface or particles or in the interparticle voids.^[30] The BET

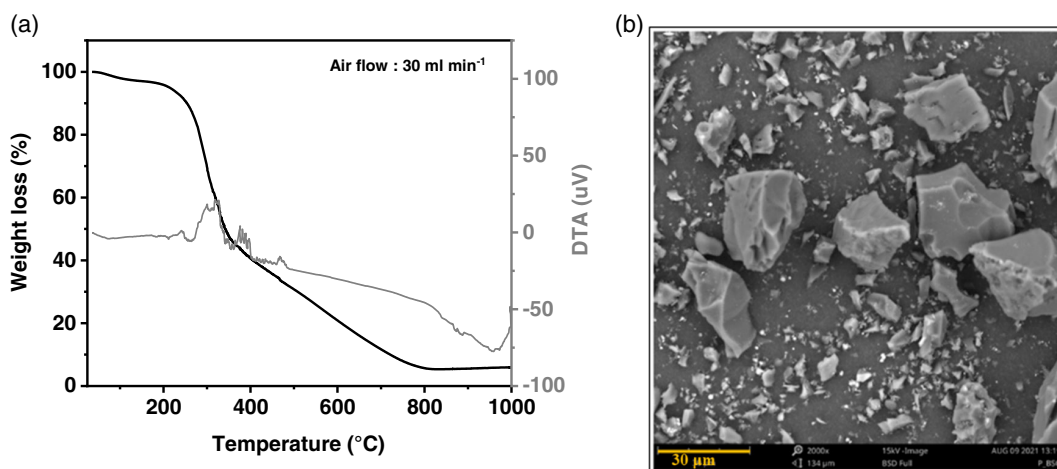


Figure 2. a) TGA/DTA analysis of BSG precursor and b) SEM image of BSG HC.

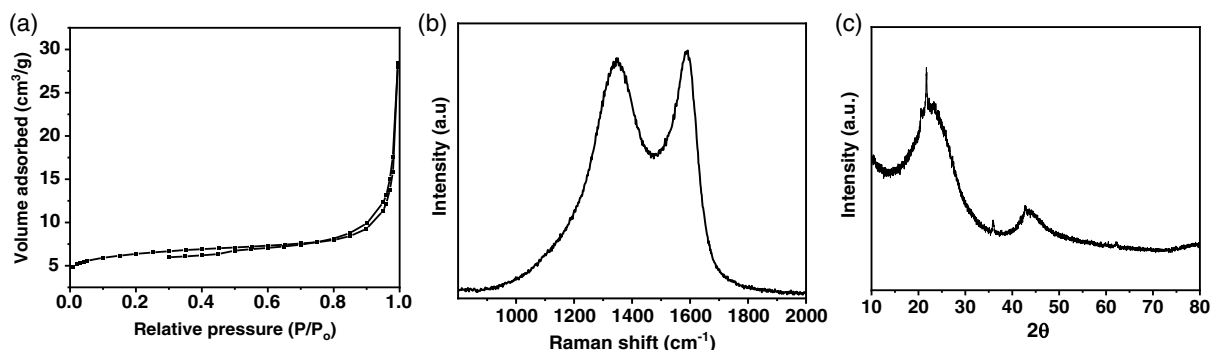


Figure 3. a) Nitrogen adsorption/desorption isotherm, b) Raman spectra, and c) powdered XRD pattern of synthesized BSG HC.

surface area is found to be $23 \text{ m}^2 \text{ g}^{-1}$, which is a value in line with those normally reported for HC (ranging between few $\text{m}^2 \text{ g}^{-1}$ to $500 \text{ m}^2 \text{ g}^{-1}$).^[18] At higher relative pressure there is marginal hysteresis corresponding to filling and emptying of mesopores by capillary condensation.

Furthermore, the HC was characterized using Raman spectroscopy. As shown in Figure 3b, two prominent peaks at 1500 and 1600 cm^{-1} corresponding to defect-induced band and graphitic band were observed. The D-band originates from breathing mode vibration of graphitic planes with defects, which is very common in HC. G-band, on the other hand, is due to relative motion of in plane sp^2 hybridized carbon, which is a very common and prominent band in graphite.^[31] The Raman spectrum is deconvoluted using Lorentzian fit and Raman intensity (I_D/I_G) is calculated to be 1.43. The ratio higher than 1 indicates the material has a defective carbon structure, which is typical for HC.^[25,29,32] According to X-ray diffraction results (Figure 3c), the material shows diffraction peaks at 20° and 45° . These peaks are correlated to the crystallographic plane of (002) and (100) in the carbon structure. The value of graphitic interlayer distance is found to be $\approx 3.84 \text{ \AA}$ calculated from (002) peak which is much larger than graphite ($\approx 3.4 \text{ \AA}$). Again, such an expanded graphitic interlayer distance is very common in HC, which is usually reported with $d(002)$ larger than 3.6 \AA . Supposedly such properties are considered favorable for de-/insertion of sodium and potassium ions.^[33] The estimated crystallite size (L_c), calculated using the Debye–Scherrer formula, is $\approx 9.7 \text{ \AA}$. In addition to carbon peaks, crystalline peaks from silica (SiO_2) nanoparticles have been identified in the diffractogram (Figure S4c, Supporting Information), which are present in barley husk as a component of plant tissue.^[34] The presence of silicon is also detected by EDX measurement (Table 1).

Table 1. BSG-derived HC properties.

Elemental composition [wt%]	Raman intensity ratio (I_D/I_G)	BET surface area	$d(002)$	L_c
Carbon 83	1.43	$21 \text{ m}^2 \text{ g}^{-1}$	0.384 nm	9.7 Å
Oxygen 15				
Silicon 1.7				

As discussed in the Introduction, HC-based electrodes are nowadays considered promising anodes for LIB, NIBs, and KIBs. For this reason, we decided to test the behavior of the composite electrodes realized utilizing the synthesized HC for these three different technologies. To the best of our knowledge, this kind of study was never considered before for BSG derived HC. With the aim to minimize the differences between these devices, we decide to test the electrodes in combination with the electrolytes 0.9 LiFSI in PC/TEG (3:7), 0.9 NaFSI in PC/TEG (3:7), and 0.9 KFSI in PC/TEG (3:7). These electrolytes display identical salt concentration and identical ratio between the solvents PC and TEG and, as shown in Figure 4, they display very comparable transport properties. As shown in the figure, at 20°C their conductivities are in order to 5 mS cm^{-1} , while their viscosities are between 5 and 6 mPa s . Taking into account these values, these electrolytes can be considered as good model electrolytes for the investigation of the HC electrodes and for the comparison of their electrochemical behavior when used as anodes for LIBs, NIBs, and KIBs.

Figure 5 shows a comparison of the CVs and charge–discharge profiles of the electrodes in the investigated electrolytes in the potential range 0.005 – 2.7 V (vs. M^+/M). As shown in the figures, the HC can be successfully utilized in all three considered electrolytes, and in all of them a reversible insertion and extraction of the metal ion (Li^+ , Na^+ , and K^+) is possible. The CV profiles (Figure 4a–c) display the typical shape of HC electrodes (in all three chemistries) and exhibit an increase in current below 1 V , resulting in a (more or less) sharp cathodic peak and anodic peak, indicating the insertion and extraction of metal ions within the carbon sample. During the first cathodic scan (≈ 3 – 0 V), two redox reactions can be distinguished, and the detected current is higher than that in the subsequent cycles. These reactions include solid–electrolyte interphase (SEI) formation and metal-ion insertion. The potential hump is a result of irreversible alkali metal-ion consumption on surface active sites, which leads to the formation of the passivation layer on the surface of electrode.^[35] In the consecutive sweep, the CV curve has overlapping cathodic and anodic peaks as a result of reversible redox reaction.

Figure 5d–f shows the charge/discharge curve of HC based in Li, Na, and K half cell at 0.1C, 0.5C and 1C ($1\text{C} = 0.372 \text{ A g}^{-1}$) in the potential range of 0.005 – 2.7 V (vs. M^+/M). Independently on the used electrolytes, the typical sloping charge/discharge profile,

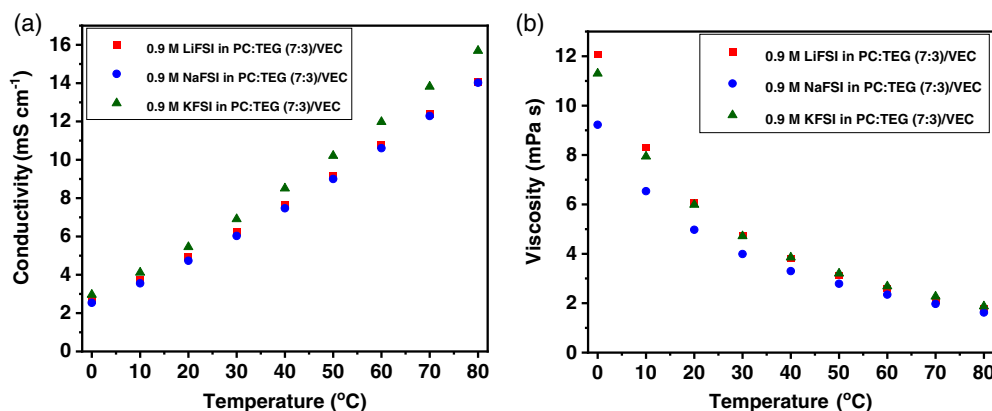


Figure 4. Comparison of a) conductivity and b) viscosity of the electrolytes 0.9 M LiFSI in PC:TEG/VEC, 0.9 M NaFSI PC:TEG/VEC, and 9 M KFSI in PC:TEG/VEC between 0 and 80 °C.

characteristic of nongraphitizing carbon,^[14] is observed. As expected, the low plateau is located to the same potential of the CV peaks discussed earlier. The efficiency of the first charge-discharge cycle (at 0.05C) is in the order of 65% in all three electrolytes but after few cycles reaches values above 96% (Figure S6a, Supporting Information). At 0.1C, the HC electrodes display a discharge capacity of 612, 265, and 294 mAh g⁻¹ in Li-, Na-, and K-based electrolyte, respectively. It is interesting to observe that while in the case of Li-based electrolyte the plateau at low potential disappears at higher current density, this is not the case for the Na-based system. This difference suggests the presence, in this latter system, of a kinetically favored storage mechanism. The electrodes cycled in the K-based electrolyte do not display a marked plateau at low potential, but they keep their profile independently on the applied current rate. These results indicate that the nature of the cation of the conducting salt of the electrolyte affects the storage mechanism occurring in the HC-based electrodes. This is not surprising as it has been widely reported that Li, Na, and K ions can be inserted and extracted through different mechanisms in host structures.^[14–17]

In order to gain further information about the different behaviors of the HC-based electrodes in the investigated electrolytes, we carried out the GITT measurement. It is important to remark that not all the boundary conditions and approximations connected to Equation (1) (see Experimental Section) are fulfilled in many real electrodes, including those used in this study. Therefore, a quantitative analysis of the results is not really possible. Nevertheless, as already reported by our^[36] and other groups,^[15,37–39] these investigations can be used to gain valuable information about the changes of the diffusion coefficient within the investigated potential and, in this specific case, about the (different) insertion–extraction process of Li, Na, and K in the investigated HC-based electrodes. As shown in **Figure 6a**, the apparent diffusion coefficient of lithium ion (D_{Li^+}) in the HC-based electrode is characterized by a slow decrease until 0.1 V versus Li⁺/Li, indicating good lithium-ion mobility inside the carbon within this voltage range. Below 0.1 V versus Li⁺/Li, a faster and substantial (one order of magnitude) decrease in D_{Li^+} occurs. This decrease can be well associated with the transition from the sloping region to the low-potential plateau

observed in the charge–discharge profiles (see Figure 5b). This change may indicate the occurrence of different storage mechanisms over the investigated range of potential. Specifically, above 0.1 V versus Li⁺/Li (sloping potential region) appears reasonable to suppose that lithium ion binds with accessible sites (defects). As suggested by many authors, this condition is energetically favored.^[14–17] Below 0.1 V versus Li⁺/Li, (plateau low potential region) a kinetic barrier arising from electrostatic repulsion during intercalation might be established, resulting in a reduction of the lithium diffusion associated with the insertion of Li ion into graphitic interlayer, as reported in the study by Alvin et al.^[15] Furthermore, the possibility of Li-ion filling inside the micropore at potential above 0 V versus Li⁺/Li, which has been found favored by small pore size and low current density,^[40] cannot be completely excluded. In a likely manner, a low-potential plateau exists at lower current density (Figure 5d) but disappears at higher current density resulting in fast decline of capacity. Since the potential range at which lithium-ion pore filling is initiated is very close to 0 V versus Li⁺/Li, the impact of cell overpotential at higher current density could prevent it from occurring. In the case of sodium, the ion diffusion appears overall lower than in the case of lithium ions, and a large variation of the diffusion coefficient over the potential is observed (Figure 6b). As shown, the D_{Na^+} is steady only until 0.4 V versus Na⁺/Na, indicating the occurrence of Na-ion capture at defective sites, heteroatoms, and functional groups^[14–17] around 0.3 V and 0.05 V versus Na⁺/Na. The turnover at 0.3 V versus Na⁺/Na could be an initiation of sodium-ion insertion into interlayers and micropores. The downturn of D_{Na^+} below 0.1 V versus Na⁺/Na followed by a turnaround falls directly in the low-potential plateau region (see Figure 5d). If the pore filling occurs at the end of plateau region, the reverse increment of diffusivity could be associated with lower kinetic barrier adsorption and clustering of metal ions inside micropores. Furthermore, the size of the cation might favor the coordination with pore walls,^[14] leading to higher pore filling potential versus M⁺/M. The decay of D_{Na^+} below 0.1 V versus Na⁺/Na could be caused by kinetically restricted sodium-ion diffusion during insertion into expanded graphitic interlayers.^[33] Figure 6c shows the variation of the diffusion coefficient observed for the potassium ions. A change of

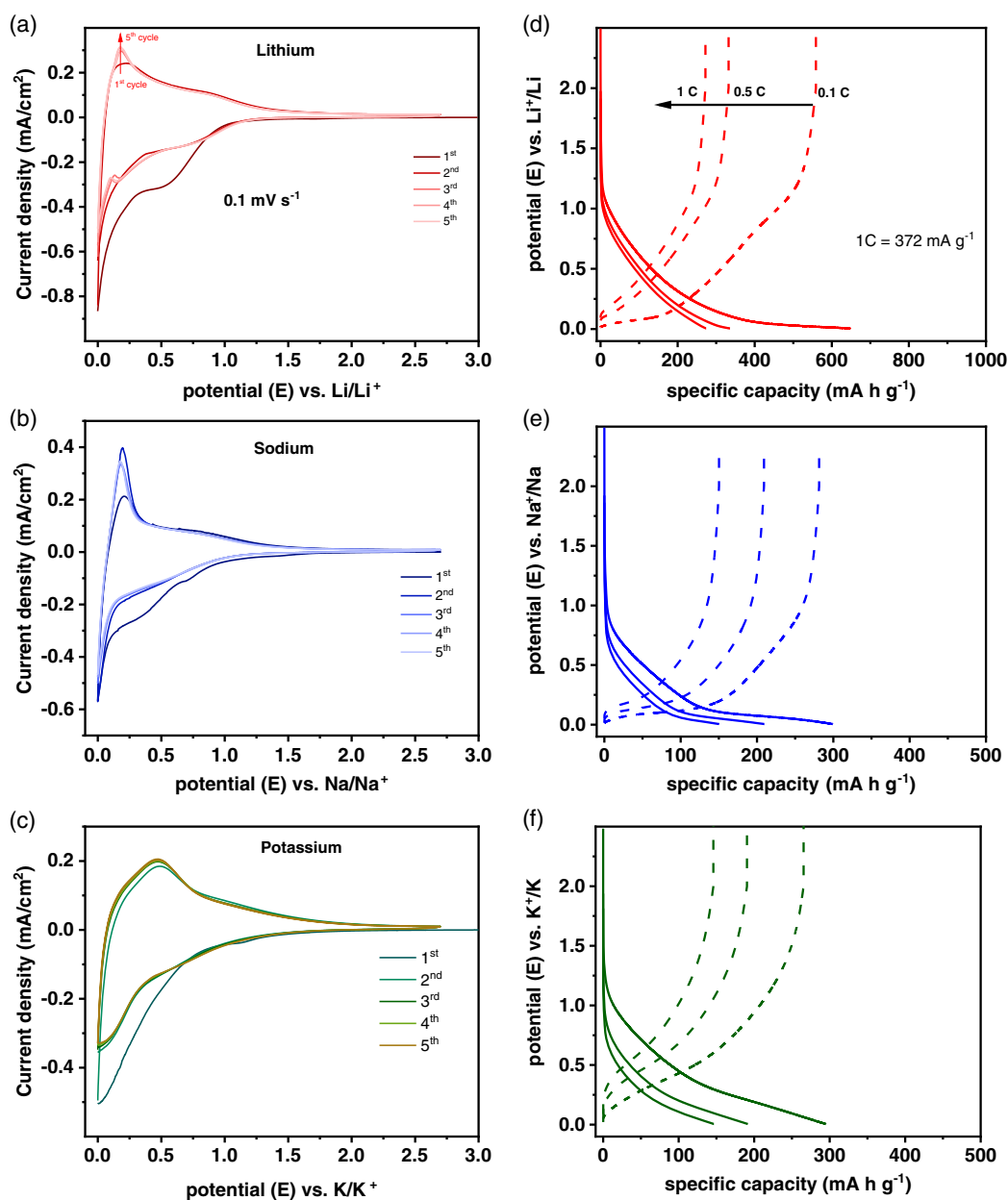


Figure 5. a–c) Cyclic voltammetry curve and d–f) galvanostatic charge/discharge profile of BSG-derived HC electrode against lithium in 0.9 M LiFSI in PC:TEG/VEC), sodium in 0.9 M NaFSI PC:TEG/VEC, and potassium in 0.9 M KFSI in PC:TEG/VEC.

diffusion process was observed at 0.4 V versus K^+/K , indicating that at this potential the adsorption storage mechanism, which is accompanied by a steady diffusivity of potassium, ends. Taking into account the ability of potassium to form intercalation compound with graphite,^[41] the possibility of potassium-ion insertion in between the graphitic interlayer of nongraphitizing carbon at low potential range cannot be neglected. Accordingly, a decline of D_{K^+} from 0.4 V versus K^+/K until 0.2 V versus K^+/K could indicate the existence of a kinetic barrier caused by repulsive electrostatic interaction and followed by insertion inside micropores until potential cutoff. Below 0.2 V versus K^+/K ,

the insertion process becomes less hindered, and the diffusion coefficient increases. These results clearly indicate that the insertion (and extraction) mechanism of lithium, sodium, and potassium within the investigated HC-based electrodes is different. Obviously, it will be important to understand these differences more in details, for example, utilizing in situ and in operando techniques. This investigation, however, is out of the scope of the present study.

After these investigations, we analyzed more in detail the electrochemical performance of the HC-based electrodes on the considered electrolytes. Specifically, we investigated the capacity

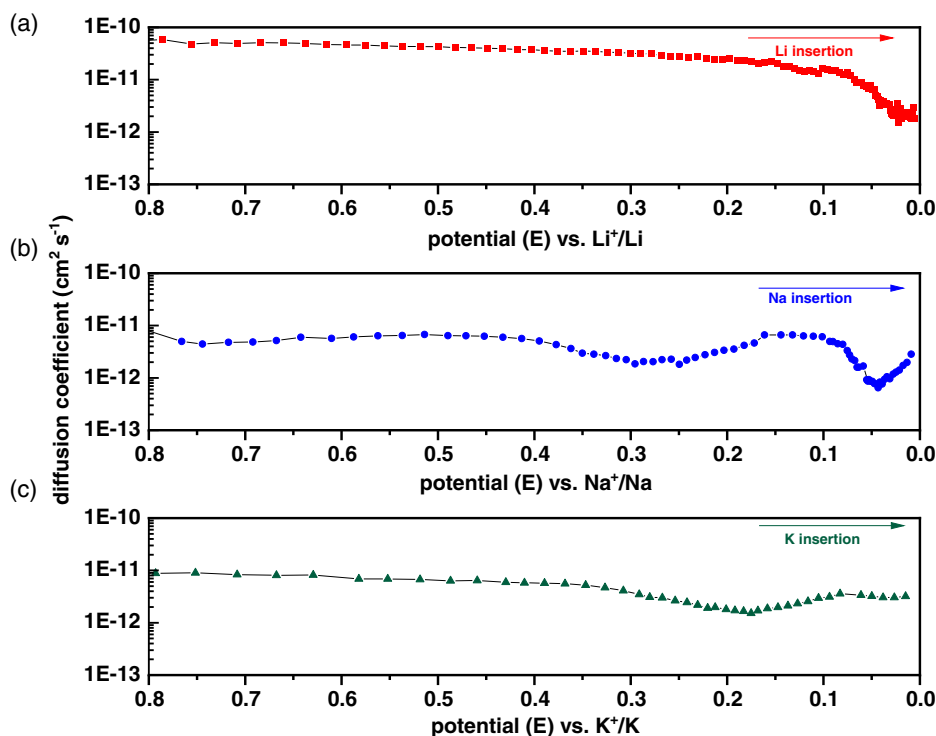


Figure 6. Apparent diffusion coefficient of a) Li, b) Na, and c) K ions in BSG-derived HC electrode as obtained from GITT measurements carried out at room temperature.

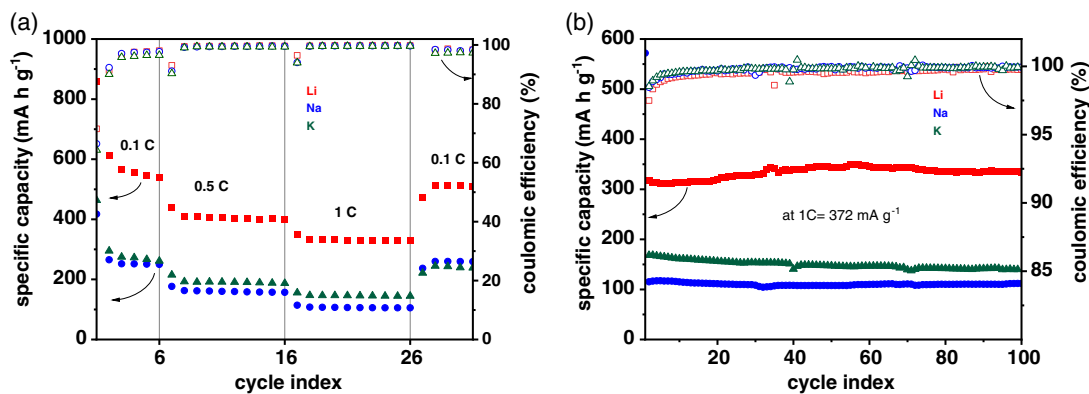


Figure 7. a) Rate test at current densities 0.1, 0.5, 1C and b) stability test at 1C rate of BSG-derived HC electrode against lithium in 0.9 M LiFSI in PC:TEG/VEC), sodium in 0.9 M NaFSI PC:TEG/VEC, and potassium in 0.9 M KFSI in PC:TEG/VEC.

retention at different C-rate and the cycling stability (at 1C). As shown in **Figure 7a**, the electrodes displayed a reversible capacity of 514, 260, and 240 mAh g^{-1} in the Li-, Na-, and K-based electrolyte, respectively, at 0.1C after rate test. When the C-rate is increased, the capacity decreased and at 1C the electrodes displayed a capacity of 330, 106, and 145 mAh g^{-1} in the Li-, Na-, and K-based electrolyte respectively. As shown in **Figure 7b**, the electrodes display very-high-capacity retention over 100 charge–discharge cycles at 1C. In the case of the Li- and Na-based electrolyte, the electrode was able to maintain 100% and 97.3% of 334 mAh g^{-1} and 97.3% 112 mAh g^{-1} (second cycle) respectively. In the case of the K-based electrolyte, the electrode

was able to retain 83 % of 168 mAh g^{-1} (second cycle). Independently of the used electrolyte, the average coulombic efficiency of the charge–discharge process was always above 99.6%, indicating a very high reversibility in all systems (**Figure S6**, Supporting Information). In spite of the simple synthesis approach, the electrochemical performance of BSG-derived HC investigated in all three alkali metal-ion batteries is comparable with state-of-the-art biomass-derived carbon reported in literature (see **Table S1**, Supporting Information).^[42–49] This result is certainly promising, especially considering that neither the electrode nor the electrolyte compositions were optimized.

4. Conclusion

In this manuscript we reported about the synthesis and characterization of HC derived from BSG, which are abundant and easily accessible biosources. We showed that using BSG, it is possible to realize HC with a suitable surface area ($21 \text{ m}^2 \text{ g}^{-1}$), particle size ($<40 \mu\text{m}$), and graphitic interlayer distance (0.384 nm) for application in practical energy storage devices. This HC can be utilized for the preparation of composite electrodes that display high-capacity, high-capacity retention at high current densities and high charge/discharge efficiency when used in combination with electrolytes suitable for LIBs, NIBs, and KIBs. Considering these promising results and taking into account that the electrode and electrolyte compositions can be further optimized, the HC derived from BSGs can be certainly considered as very promising materials for the realization of advanced metal-ion batteries.

Supporting Information

Supporting Information is available from the Wiley Online Library or from the author.

Acknowledgements

S.D.M., C.L., and A.B. wish to thank the Deutsche Forschungsgemeinschaft (DFG) (project BA4956/21-1), the Thüringer Ministerium für Wirtschaft, Wissenschaft und Digitale Gesellschaft (TMWWDG) and the Thüringer Aufbau Bank (TAB) within the project LiNaKon (2018 FGR 0092) for financial support. The authors wish to thank the brewery "Jena Papiermühle" for providing spent grain sample.

Open Access funding enabled and organized by Projekt DEAL.

Conflict of Interest

The authors declare no conflict of interest.

Data Availability Statement

The data that support the findings of this study are available from the corresponding author upon reasonable request.

Keywords

biomass, Brewer's spent grains, hard carbon, metal-ion batteries

Received: April 13, 2022

Revised: June 24, 2022

Published online: July 19, 2022

- [1] N. Nitta, F. Wu, J. T. Lee, G. Yushin, *Mater. Today* **2015**, *18*, 252.
- [2] T. Chen, Y. Jin, H. Lv, A. Yang, M. Liu, B. Chen, Y. Xie, Q. Chen, *Trans. Tianjin Univ.* **2020**, *26*, 208.
- [3] Y. Sun, X.-L. Shi, Y.-L. Yang, G. Suo, L. Zhang, S. Lu, Z.-G. Chen, *Adv. Funct. Mater.* **2022**.
- [4] N. Soltani, A. Bahrami, L. Giebeler, T. Gemming, D. Mikhailova, *Prog. Energy Combust. Sci.* **2021**, *87*, 100929.

- [5] B. Escobar, D. C. Martínez-Casillas, K. Y. Pérez-Salcedo, D. Rosas, L. Morales, S. J. Liao, L. L. Huang, X. Shi, *Int. J. Hydrogen Energy* **2021**, *46*, 26053.
- [6] W. Xing, J. S. Xue, J. R. Dahn, *J. Electrochem. Soc.* **1996**, *143*, 3046.
- [7] E. Irisarri, N. Amini, S. Tennison, C. M. Ghimbeu, J. Gorka, C. Vix-Guterl, A. Ponrouch, M. R. Palacin, *J. Electrochem. Soc.* **2018**, *165*, A4058.
- [8] Z.-L. Yu, S. Xin, Y. You, L. Yu, Y. Lin, D.-W. Xu, C. Qiao, Z.-H. Huang, N. Yang, S.-H. Yu, J. B. Goodenough, *J. Am. Chem. Soc.* **2016**, *138*, 14915.
- [9] A. Kamiyama, K. Kubota, T. Nakano, S. Fujimura, S. Shiraishi, H. Tsukada, S. Komaba, *ACS Appl. Energy Mater.* **2020**, *3*, 135.
- [10] P. Bai, Y. He, P. Xiong, X. Zhao, K. Xu, Y. Xu, *Energy Storage Mater.* **2018**, *13*, 274.
- [11] Y. Li, K. Xiao, C. Huang, J. Wang, M. Gao, A. Hu, Q. Tang, B. Fan, Y. Xu, X. Chen, *Nano-Micro Lett.* **2021**, *13*, 1.
- [12] L. Xie, C. Tang, Z. Bi, M. Song, Y. Fan, C. Yan, X. Li, F. Su, Q. Zhang, C. Chen, *Adv. Energy Mater.* **2021**, *11*, 2101650.
- [13] E. Olsson, J. Cottom, Q. Cai, *Small* **2021**, *17*, 2007652.
- [14] Y. Huang, Y. Wang, P. Bai, Y. Xu, *ACS Appl. Mater. Interfaces* **2021**, *13*, 38441.
- [15] S. Alvin, H. S. Cahyadi, J. Hwang, W. Chang, S. K. Kwak, J. Kim, *Adv. Energy Mater.* **2020**, *10*, 2070093.
- [16] H. Euchner, B. P. Vinayan, M. A. Reddy, M. Fichtner, A. Groß, *J. Mater. Chem. A* **2020**, *8*, 14205.
- [17] X.-Q. Cheng, H.-J. Li, Z.-X. Zhao, Y.-Z. Wang, X.-M. Wang, *Xinxing Tan Cailiao/New Carbon Mater.* **2021**, *36*, 93.
- [18] P. Yu, W. Tang, F.-F. Wu, C. Zhang, H.-Y. Luo, H. Liu, Z.-G. Wang, *Rare Met.* **2020**, *39*, 1019.
- [19] E. M. Lotfabad, J. Ding, K. Cui, A. Kohandehghan, W. P. Kalisvaart, M. Hazelton, D. Mitlin, *ACS Nano* **2014**, *8*, 7115.
- [20] N. Zhang, Q. Liu, W. Chen, M. Wan, X. Li, L. Wang, L. Xue, W. Zhang, *J. Power Sources* **2018**, *378*, 331.
- [21] W. Cao, E. Zhang, J. Wang, Z. Liu, J. Ge, X. Yu, H. Yang, B. Lu, *Electrochim. Acta* **2019**, *293*, 364.
- [22] S. I. Mussatto, G. Dragone, I. C. Roberto, *J. Cereal Sci.* **2006**, *43*, 1.
- [23] Eurostat, Happy International Beer Day! **2019**. <https://ec.europa.eu/eurostat/product?code=EDN-20200807-1>.
- [24] K. M. Lynch, E. J. Steffen, E. K. Arendt, *Brewers' spent grain: a review with an emphasis on food and health*, pp. 553–568, **2016**.
- [25] Y. Feng, L. Tao, Y. He, Q. Jin, C. Kuai, Y. Zheng, M. Li, Q. Hou, Z. Zheng, F. Lin, H. Huang, *J. Mater. Chem. A* **2019**, *7*, 26954.
- [26] W. Weppner, R. A. Huggins, *J. Electrochem. Soc.* **1977**, *124*, 1569.
- [27] H. Yang, *Fuel* **2007**, *86*, 1781.
- [28] H. L. Ornaghi, F. G. Ornaghi, R. M. Neves, F. Monticeli, O. Bianchi, *Cellulose* **2020**, *27*, 4949.
- [29] A. Patat, *Chem. Commun.* **2018**, *50*, 181.
- [30] M. Thommes, K. Kaneko, A. V. Neimark, J. P. Olivier, F. Rodriguez-Reinos, J. Rouquerol, K. S. W. Sing, *Pure Appl. Chem.* **2015**, *87*, 1051.
- [31] A. C. Ferrari, J. Robertson, *Phys. Rev. B - Condens. Matter Mater. Phys.* **2000**, *61*, 14095.
- [32] D. B. Schuepfer, F. Badaczewski, J. M. Guerra-Castro, D. M. Hofmann, C. Heiliger, B. Smarsly, P. J. Klar, *Carbon NY* **2020**, *161*, 359.
- [33] Y. Wen, K. He, Y. Zhu, F. Han, Y. Xu, I. Matsuda, Y. Ishii, J. Cumings, C. Wang, *Nat. Commun.* **2014**, *5*, 1.
- [34] E. Akhayere, D. Kavaz, A. Vaseashta, *Polish J. Environ. Stud.* **2019**, *28*, 2513.
- [35] E. Peled, S. Menkin, *J. Electrochem. Soc.* **2017**, *164*, A1703.
- [36] C. Leibing, A. Balducci, *J. Electrochem. Soc.* **2021**, *168*, 090533.
- [37] Y. Li, Y. S. Hu, M. M. Titirici, L. Chen, X. Huang, *Adv. Energy Mater.* **2016**, *6*, 1.

- [38] P. Wang, K. Zhu, K. Ye, Z. Gong, R. Liu, K. Cheng, G. Wang, J. Yan, D. Cao, *J. Colloid Interface Sci.* **2020**, *561*, 203.
- [39] P. Wang, X. Zhu, Q. Wang, X. Xu, X. Zhou, J. Bao, *J. Mater. Chem. A* **2017**, *5*, 5761.
- [40] J. Hu, H. Li, X. Huang, *Solid State Ionics* **2005**, *176*, 1151.
- [41] K. Share, A. P. Cohn, R. E. Carter, C. L. Pint, *Nanoscale* **2016**, *8*, 16435.
- [42] D. Kang, H.-K. Kim, H.-J. Kim, Y. Han, *J. Alloys Compd.* **2022**, *900*, 163420.
- [43] T. J. Yokokura, J. R. Rodriguez, V. G. Pol, *ACS Omega* **2020**, *5*, 19715.
- [44] M. Drews, J. Büttner, M. Bauer, J. Ahmed, R. Sahu, C. Scheu, S. Vierrath, A. Fischer, D. Biro, *ChemElectroChem* **2021**, *8*, 4750.
- [45] Y. Li, H. Shi, C. Liang, K. Yu, *Ionics* **2021**, *27*, 1025.
- [46] S. Chen, K. Tang, F. Song, Z. Liu, N. Zhang, S. Lan, X. Xie, Z. Wu, *Nanotechnology* **2022**, *33*, 055401.
- [47] U. Kumar, J. Wu, N. Sharma, V. Sahajwalla, *Energy Fuels* **2021**, *35*, 1820.
- [48] M. Yang, J. Dai, M. He, T. Duan, W. Yao, *J. Colloid Interface Sci.* **2020**, *567*, 256.
- [49] H. D. Pham, K. Mahale, T. M. L. Hoang, S. G. Mundree, P. Gomez-Romero, D. P. Dubal, *ACS Appl. Mater. Interfaces* **2020**, *12*, 48518.